

See discussions, stats, and author profiles for this publication at: <https://www.researchgate.net/publication/313768300>

Non-uniform temperature and species concentration measurements in a laminar flame using multi-band infrared absorption spectroscopy

Article in *Applied Physics B* · March 2017

DOI: 10.1007/s00340-017-6645-7

CITATIONS

21

READS

310

3 authors, including:



Lihao Ma

The Chinese University of Hong Kong

29 PUBLICATIONS 81 CITATIONS

[SEE PROFILE](#)



Lok Yin Lau

The Chinese University of Hong Kong

2 PUBLICATIONS 21 CITATIONS

[SEE PROFILE](#)

Some of the authors of this publication are also working on these related projects:



Laser Diagnostics for Transient Combustion Phenomena [View project](#)



Temperature/Species concentration sensing in laminar and turbulent flames using tunable diode laser absorption spectroscopy [View project](#)



Non-uniform temperature and species concentration measurements in a laminar flame using multi-band infrared absorption spectroscopy

Liu Hao Ma¹ · Lok Yin Lau¹ · Wei Ren^{1,2} 

Received: 16 November 2016 / Accepted: 12 January 2017 / Published online: 8 March 2017
© Springer-Verlag Berlin Heidelberg 2017

Abstract We report in situ measurements of non-uniform temperature, H₂O and CO₂ concentration distributions in a premixed methane–air laminar flame using tunable diode laser absorption spectroscopy (TDLAS). A mid-infrared, continuous-wave, room-temperature interband cascade laser (ICL) at 4183 nm was used for the sensitive detection of CO₂ at high temperature. The H₂O absorption lines were exploited by one distributed feedback (DFB) diode laser at 1343 nm and one ICL at 2482 nm to achieve multi-band absorption measurements with high species concentration sensitivity, high temperature sensitivity, and immunity to variations in ambient conditions. A novel profile-fitting function was proposed to characterize the non-uniform temperature and species concentrations along the line-of-sight in the flame by detecting six absorption lines of CO₂ and H₂O simultaneously. The flame temperature distribution was measured at different heights above the burner (5–20 mm), and compared with the thermocouple measurement with heat-transfer correction. Our TDLAS measured temperature of the central flame was in excellent agreement (<1.5% difference) with the thermocouple data. The TDLAS results were also compared with the CFD simulations using a detailed chemical kinetics mechanism (GRI 3.0) and considering the heat loss to the surroundings. The current CFD simulation overpredicted the flame temperature in the gradient region, but was in excellent agreement

with the measured temperature and species concentration in the core of the flame.

1 Introduction

The flat flame burner, generating laminar premixed flame with good temporal stability and spatial uniformity at lean and rich conditions, has been extensively used to study combustion physics and chemistry, as well as to validate novel optical diagnostic techniques [1–3]. Accurate knowledge of the flame temperature is key to providing experimental data with high fidelity for combustion research. A thermocouple is frequently used for temperature measurement but has the issue of introducing interference to the flow field. Measurement corrections are always required to account for the radiation heat transfer between the thermocouple wire and the cool surroundings, leading to unavoidable uncertainties in the temperature measurement.

Non-intrusive laser-based diagnostics of temperature and species concentration include planar laser-induced fluorescence (PLIF), coherent anti-Stokes Raman scattering (CARS), and tunable diode laser absorption spectroscopy (TDLAS). Among these optical diagnostics, PLIF can provide temporally and spatially resolved information of temperature and species concentration [4]. The combination of particle image velocimetry (PIV) and PLIF enabled the simultaneous measurement of the velocity and species concentration [5]. The accuracy of PLIF relies on the temperature calibration and the spectral properties of the dye. The fluorescence interferences sometimes occur during the measurement of species concentration in the combustion system [6]. CARS has the advantages of the high signal level, good sensitivity and spatial resolution [7], which was successfully applied in the diagnostics of temperature in a

✉ Wei Ren
renwei@mae.cuhk.edu.hk

¹ Department of Mechanical and Automation Engineering, The Chinese University of Hong Kong, New Territories, Hong Kong

² Shenzhen Research Institute, The Chinese University of Hong Kong, New Territories, Hong Kong

scramjet [8, 9]. However, CARS is sensitive to the background fluorescence noise and the phase mismatch caused by the refractive index variation in the optical path. Hence, PLIF and CARS could provide spatially resolved measurements of temperature and species concentrations of the combustion flow, but require relatively complicated optical setup and expensive light sources (i.e., Nd:YAG and dye laser). Additionally, their sensitivity to the background noise and the inevitable temperature calibration process make both techniques difficult to achieve quantitative measurements with high fidelity.

TDLAS has been widely used in combustion diagnostics due to its advantages of highly quantitative measurement and relatively simple optical setup. For instance, the up-to-date laser sources enabled the accurate measurements of the time-histories of fuel, intermediate and product species in the combustion system using TDLAS [3]. Among the various TDLAS sensors, the near-infrared distributed feedback (DFB) diode lasers (1.3–1.5 μm) were mostly adopted in the flame measurement [10–12] because of the matured telecommunication laser technologies.

In the previous TDLAS measurement of flame temperature, the uniform distributions of temperature and species concentrations were commonly assumed along the line-of-sight (LOS). The measured temperature using two-line thermometry and species concentration could only be treated as an averaged result along the LOS. However, the actual combustion flow field involves significant non-uniformity particularly due to the thermal boundary layer, heat transfer effect, and chemical reactions. Even for the simplest case of a laminar flat flame, the thermocouple and CARS measurements verified that the quasi-uniform condition exists only in the very narrow central region [13, 14]. The ignorance of non-uniformity in the flame could lead to large uncertainties in the TDLAS measurements. For instance, Zhou et al. [15] discovered that the averaged LOS result was consistently 140 K lower than the thermocouple measurement for a flat diffusion flame. Goldenstein [16] conducted the spectral absorption simulation of H_2O for a representative hydrogen-air flame and proved the non-uniformity was inevitable according to the discrepancy between the path-integrated and the path-averaged results. Hence, the averaged LOS measurement is no longer applicable to the combustion field with significant temperature and species gradients.

Various studies were conducted to quantify the non-uniform issues in the flame using the TDLAS method. The traditional two-line thermometry only requires two absorption lines to derive the average temperature and species concentration for the uniform medium. However, the non-uniformity in the flame significantly increases the number of unknown parameters (i.e., temperature and species concentration) along the LOS. The “effective

absorption path” and “curve-fit” methods were first proposed by Ouyang and Varghese to correct the boundary layer effect [17]. Later on, Sanders et al. [18] reported the multi-line thermometry using a series of distinct absorption lines to derive the distributions of temperature and species concentration. Liu [19] systematically investigated the multi-line thermometry method by proposing the profile-fitting and temperature-binning strategies to characterize the non-uniform distributions of temperature and H_2O concentration in a flat flame. The 2-T and trapezoid profiles were proposed in the profile-fitting process. In the 2-T profile fitting of temperature, only the core flame and the co-flow region were characterized without considering the gradient width from the core flame to the co-flow. On the other hand, the trapezoid fitting profile described the temperature distribution from the core flame with a linear transition to the co-flow region. The 2-T and trapezoid profiles were applied to characterize the flame non-uniformity in the Stanford long flat flame burner and Hencken burner [19, 20]. Recently, Zhang et al. [21] and Liu et al. [22] utilized the temperature-binning strategy to measure the non-uniformity of a flat flame by exploiting the H_2O absorption lines in the near infrared. Additionally, the TDLAS-based tomography reconstruction method was proved an efficient method to spatially resolve the non-uniformity of the combustion field [23–26]. In this method, the directional information of the LOS absorption was obtained to reconstruct the spatially resolved distributions of temperature and species concentration using the standard reconstruction methods (i.e., multiplicative algebraic reconstruction technique). Note that the tomography method normally requires sophisticated mathematical retrieval methods and laser diagnostic systems with sufficient optical accesses.

Hence, TDLAS offers an opportunity to obtain the non-uniform flame temperature and species concentrations with a simpler optical setup, faster time response, and more quantitative measurements compared with PLIF and CARS techniques. In the case of the laminar flame with an axial symmetry, a more appropriate profile-fitting function is required to describe the non-uniform combustion flow field. In this work, we report the development of a novel multi-band infrared absorption strategy for the characterization of non-uniform temperature, H_2O and CO_2 distributions in a flat flame. Instead of the simplified 2-T or trapezoid distribution profile, a new fitting function was proposed to better characterize the non-uniformity of the flat flame. Besides the telecommunication near-infrared diode laser, we employed the additional mid-infrared, room-temperature, interband cascade lasers (ICLs) for the more sensitive laser absorption measurement. More specifically, we used the 4.2 μm ICL to measure CO_2 absorption, and the 2.5 μm ICL and 1.3 μm diode laser to monitor H_2O absorption. The cross-band absorption

measurement of H_2O and CO_2 in the near-IR and mid-IR enables more sensitive and precise temperature and species detection.

2 Theoretical background

2.1 Spectroscopic fundamental

Laser absorption spectroscopy is governed by the well-known Beer–Lambert law. When a laser beam passes through a gas medium with a length of L (cm), the fractional transmission can be expressed as [27]:

$$\left(\frac{I_t}{I_0}\right)_v = \exp(-k_v L) = \exp\left(-P \int_0^L X_{\text{abs}}(x) S_i(T(x)) \phi_v dx\right) \quad (1)$$

where I_0 and I_t are the incident and transmitted laser intensity, respectively; $X_{\text{abs}}(x)$ is the concentration of the absorbing gas, P is the static pressure, $S(T(x))$ is the line-strength of the transition which is only a function of temperature T , and ϕ_v is the line-shape function. The product $k_v \cdot L$ is known as the spectral absorbance and k_v is the absorption coefficient. Because the line-shape function ϕ_v is normalized, the integrated absorbance across the absorption feature can be obtained:

$$A = \int_{-\infty}^{\infty} k_v L dv = P \int_0^L X_{\text{abs}}(x) S_i(T(x)) dx \quad (2)$$

The profile-fitting strategy is applied to characterize the non-uniform temperature and concentration distributions [19] considering the axisymmetrical property of the flat flame above the McKenna burner. In this method, the integrated areas of the selected absorption lines are obtained based on the proposed temperature and species distribution profiles. If m transitions of a single species or multi-species are selected for the absorption measurement, a set of equations can be established as:

$$\begin{cases} A_1 = P \int_0^L X_{\text{abs}}(x) S_1(T(x)) dx \\ A_i = P \int_0^L X_{\text{abs}}(x) S_i(T(x)) dx \\ \vdots \\ A_m = P \int_0^L X_{\text{abs}}(x) S_m(T(x)) dx \end{cases} \quad (3)$$

where $T(x)$ and $X_{\text{abs}}(x)$ are the temperature and species concentration distributions along the optical path, respectively. The equations above can be solved by the nonlinear least-square fitting method:

$$\min_{T(x), X_{\text{abs}}(x)} \sum_{i=1}^m \left(\frac{P \int_0^L X_{\text{abs}}(x) S_i(T(x)) dx - A_{\text{measured}}^i}{A_{\text{measured}}^i} \right)^2 \quad (4)$$

In particular, we selected H_2O and CO_2 as the diagnostic targets in this study and the nonlinear least-square fitting above can be expressed as:

$$\min_{T(x), X_{\text{H}_2\text{O}}(x), X_{\text{CO}_2}(x)} \left(\sum_{i=1}^m \left(\frac{P \int_0^L X_{\text{H}_2\text{O}}(x) S_i(T(x)) dx - A_{\text{H}_2\text{O}}^i}{A_{\text{H}_2\text{O}}^i} \right)^2 + \sum_{j=1}^n \left(\frac{P \int_0^L X_{\text{CO}_2}(x) S_j(T(x)) dx - A_{\text{CO}_2}^j}{A_{\text{CO}_2}^j} \right)^2 \right) \quad (5)$$

The nonlinear least-square fitting process was carried out iteratively by the enumeration method to cover all the unknown parameters. Note that the calculation resolution of the central uniform temperature and $\text{H}_2\text{O}/\text{CO}_2$ concentration is 1 K and 0.001, respectively.

2.2 Temperature/species distribution profile

The laminar flame with cold boundary condition was previously modeled using the simplified 2-T or trapezoid profile. Both profiles were only valid for the flat flame with a negligible gradient zone [19]. However, it is not true for the case of McKenna burner with cold shielding nitrogen that tends to generate a gradient zone with its length comparative to that of the flame core with a uniform temperature. Hence, the non-uniform temperature and species concentration distributions cannot be accurately characterized by the over-simplified 2-T or trapezoid profile. In other words, these two distribution profiles cannot describe the non-uniform distributions of temperature and species concentration caused by the thermal conduction, as well as the convection and radiation between the flame, shielding gas and the ambient.

A more appropriate distribution profile is required to accurately describe the non-uniform temperature and species concentration distributions while implementing the profile fitting strategy in the TDLAS measurement. Here a Boltzmann fitting profile is proposed based on the thermocouple measurement results; further detail of the thermocouple measurement is discussed in the following section. The Boltzmann profile can be expressed as:

$$y = A_2 + \frac{A_1 - A_2}{1 + e^{(x-x_0)/A_3}} \quad (6)$$

If y designates the flame temperature, the parameter A_1 is the central uniform temperature, A_2 is the ambient temperature, A_3 is a constant describing the level of transition gradient, and x_0 indicates the radial position where the flame temperature is equal to $(A_1 - A_2)/2$.

Figure 1 compares the thermocouple measurement with the fitting results of the radial flame temperature using the

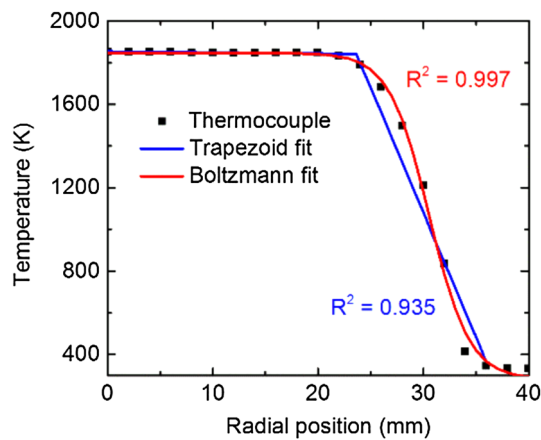


Fig. 1 Comparison of the thermocouple data with the fitting results using the trapezoid and Boltzmann functions

trapezoid and Boltzmann functions, respectively. Note that the thermocouple data shown in Fig. 1 was directly adopted from the McKenna burner used in this study. It is evident that the fitting result using the Boltzmann profile shows better agreement with the thermocouple measurement according to the higher R-square value. Thus, the more proper fitting function used in the nonlinear least-square fitting process can lead to a better retrieval of the non-uniform distribution of flame temperature and species concentration.

3 Experimental and CFD modeling

All experiments were performed in a premixed methane-air flame (water-cooled McKenna burner) stabilized above a sintered stainless-steel porous disk with a diameter of 60 mm. The flame was shielded by nitrogen coming from the sintered bronze shroud ring to eliminate the ambient interference. The height of the burner surface relative to the optical table could be adjusted in the range of 0–50 mm so that the laser diagnostics could be conducted at different heights above the burner (HAB). The supplied methane, air and nitrogen have a purity of 99.99% (YaTai), 99.99% (with $\text{H}_2\text{O} < 20$ ppm, Linde) and 99.999% (Linde), respectively. A check valve was installed in the burner to prevent backflow and a flashback arrestor was installed at the outlet of the methane cylinder. All the flow rates were monitored by the calibrated rotameters.

3.1 TDLAS optical setup

The schematic of the TDLAS setup is depicted in Fig. 2. Two tunable continuous-wave (CW) ICLs of 2482 and 4183 nm (Nanoplus) and one near-infrared diode laser of 1343 nm (Qingchen) were employed as the light sources. The temperature and injection current of each laser were

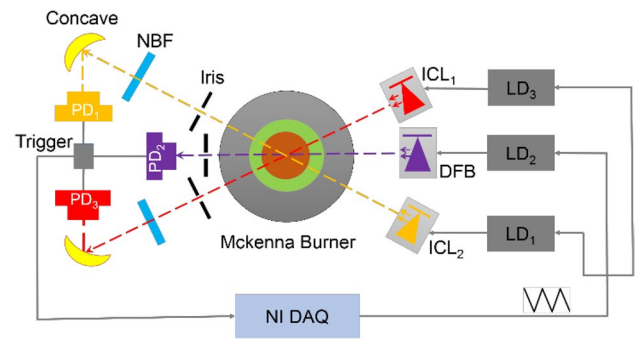


Fig. 2 Schematic of the TDLAS experimental setup in the premixed flame. ICL_1 interband cascade laser, 2482 nm; ICL_2 interband cascade laser, 4183 nm; DFB distributed-feedback diode laser, 1343 nm; PD photodetector; NBF narrow-bandpass filter; LD laser driver

controlled by the commercial laser drivers (Wavelength Electronics). The wavelength tuning performance was characterized by two infrared spectrometers, Bristol 771B for mid-infrared and Yokogawa AQ6370D for near-infrared. A Ge-etalon (3-inch in length) was used for the calibration of the relative wavelength scanning. The laser wavelength was scanned using the LabVIEW generated triangle function wave to cover the selected absorption lines.

A spectral simulation of the selected absorption lines using the HITRAN database [28] was plotted in Fig. 3. These absorption lines belong to either the $\nu_1 + \nu_3$ and ν_3 vibrational bands of H_2O , or the ν_3 band of CO_2 . The six absorption lines were selected based on the systematic selection criteria documented in reference [20], such as strong line-strength to guarantee high SNR, minimal interference from ambient water vapor, well-separated lower state energies E'' to provide high temperature sensitivity, and good isolation from neighboring transitions. Note that the selected transitions must have negligible absorption at room temperature compared with that at flame temperature. If a transition has a strong absorption

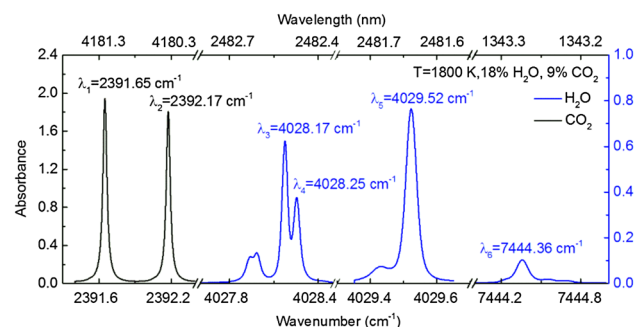


Fig. 3 Spectral simulation of the selected six absorption lines of H_2O and CO_2 in the wavelength range of 1.34–4.18 μm . Simulation condition: 1800 K, 1 atm, 6 cm path length, 18% H_2O and 9% CO_2

coefficient at room temperature, the measurement accuracy is compromised by the interfering absorption of the ambient species (H_2O or CO_2) along the line-of-sight outside the flame region. Hence, we used the transitions with relatively large lower state energy ($E'' > 1780 \text{ cm}^{-1}$) to ensure that the absorption at room temperature is much smaller than that at flame temperature. Additionally, the selected strong H_2O transitions in the $\nu_1 + \nu_3$ and ν_3 vibrational bands have a difference of 875 cm^{-1} in the lower state energy E'' , leading to a sufficient temperature sensitivity over the typical flame temperature of 1500–2000 K. Spearrin et al. [29] previously demonstrated the use of multi-band infrared absorption spectroscopy of CO_2 to achieve an accuracy of temperature measurement better than 1% in shock tube experiments. The combination of multiple absorption bands of H_2O and CO_2 in this work will enable high detection sensitivity and SNR for temperature and species concentration measurements.

All three lasers were directed through the flat flame at the same HAB as illustrated in Fig. 2. The intersection of the three LOS was located at the center of the burner. The same temperature/species distribution along the three optical paths was assumed considering the axial symmetry of the McKenna burner. The transmitted laser radiation was collected by the concave mirror and focused onto the photodetector. Additionally, we placed the iris and narrowband optical filters (Spectrogon, $<80 \text{ nm}$ bandwidth) in the optical path to mitigate the thermal background signal from the flame radiation. A multi-channel data acquisition module (National Instrument) performed the signal trigger synchronization, data acquisition and analysis.

3.2 CFD modeling

The CFD simulation was conducted for the comparison with the experimental results using the FLUENT module in ANSYS software. The dimension and grid of the computational domain for the flame used in this study are described in Fig. 4. Note that only half of the computational domain was considered for simulation, which was discretized into 17,536 quadrilateral cells. The GRI 3.0 mechanism [30] was adopted in the chemistry solving process. Regarding the boundary condition settings, we set the mixed fuel inlet and shielding gas inlet as the velocity inlets, and the outlet boundaries of the computational domain as the pressure outlets with zero gauge pressure.

In the CFD simulation, we employed the pressure-based solver, the SIMPLE algorithm and the second-order upwind scheme for the detailed calculation. The flow rates of the methane and air were set to 1.5 and 15.0 L/min (equivalence ratio of ~ 1). The flow rate of the shielding gas was maintained at 10.0 L/min to stabilize the flame. All the flow rates were set the same as the experimental conditions.

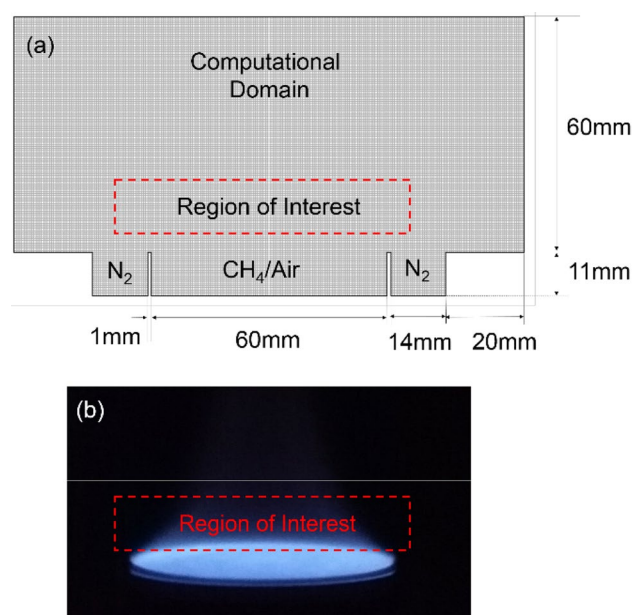


Fig. 4 **a** The computational domain of the burner for the CFD simulation. **b** A photograph of the actual flame at the stoichiometric condition

The region of interest for both simulation and measurement ranges from HAB = 5 mm to 20 mm as indicated in Fig. 4.

4 Results and discussion

The representative measurement of the absorption spectra of H_2O and CO_2 is plotted in Fig. 5 along with the corresponding Voigt-fitting profiles. All these absorption features with high SNR can be well fitted using Voigt line-shapes. In particular, the Voigt-fitting residuals of the selected four H_2O lines (Fig. 5a–c) are measured to be $<2.2\%$, and $<1\%$ for those two CO_2 lines (Fig. 5d). Note that the residuals are mainly associated with the measurement uncertainties and the fitting errors of the absorption features with multiple Voigt functions. The integrated area of each feature is thus obtained to characterize the non-uniform temperature and species distributions in the flame.

In comparison, a fine gage B-type (platinum-30% rhodium/platinum-6% rhodium) thermocouple (Omega) with a diameter of 0.254 mm was used to measure the radial temperature at various HABs. Note that the correction of the thermocouple reading must be performed to account for the effect of heat transfer. In particular, the thermocouple data acquired by the monitor were corrected by taking into account the thermocouple reading error (around 0.5%) and the heat-transfer correction (around 5%) [31]. Considering the central flame temperature of $\sim 1800 \text{ K}$, the corrected

Fig. 5 Measured absorption spectra of (a) H₂O near 2.5 μm , (b) H₂O near 2.5 μm , (c) H₂O near 1.3 μm , and (d) CO₂ near 4.2 μm , at HAB = 5 mm. The Voigt fit to the experimental data is plotted for comparison along with the residual

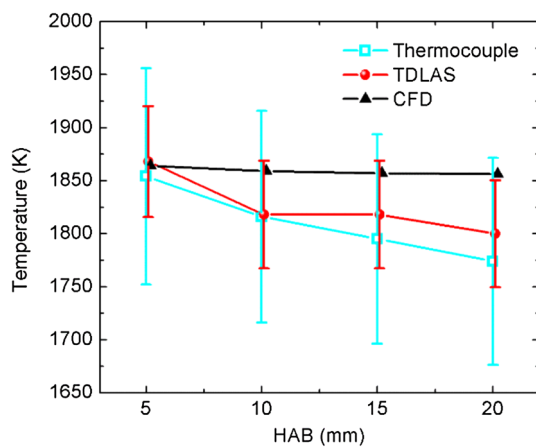
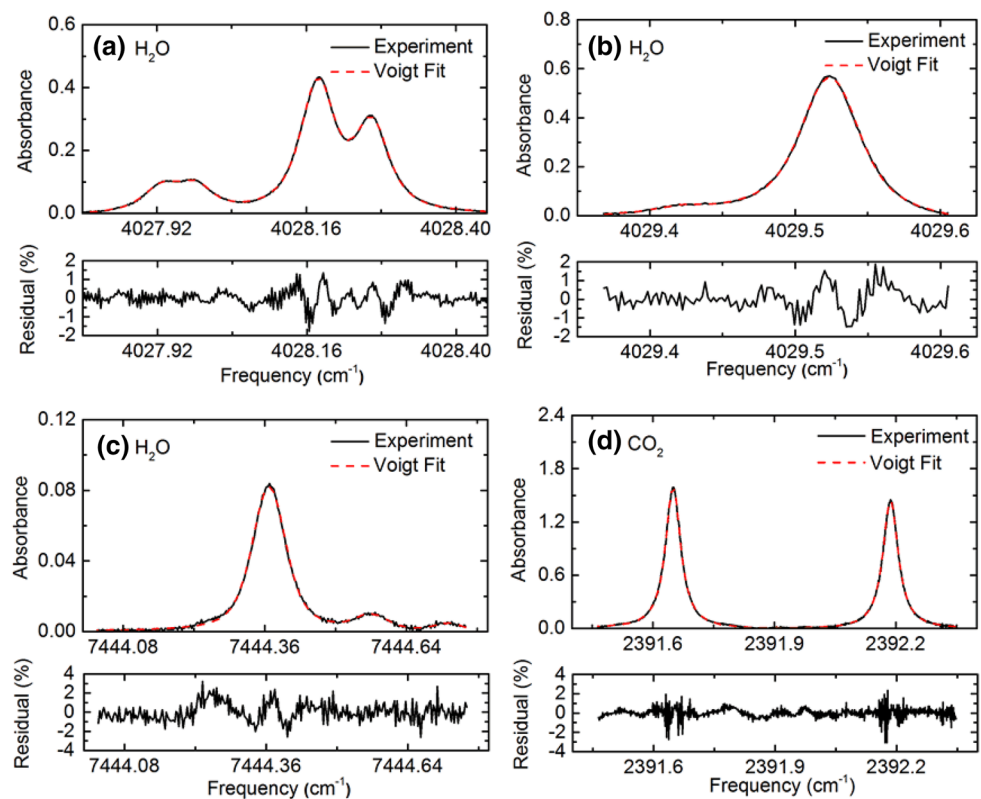


Fig. 6 Comparison of the central flame temperature obtained using TDLAS and thermocouple measurements with the CFD simulation at various HAB. The error bar for CFD simulation is not shown

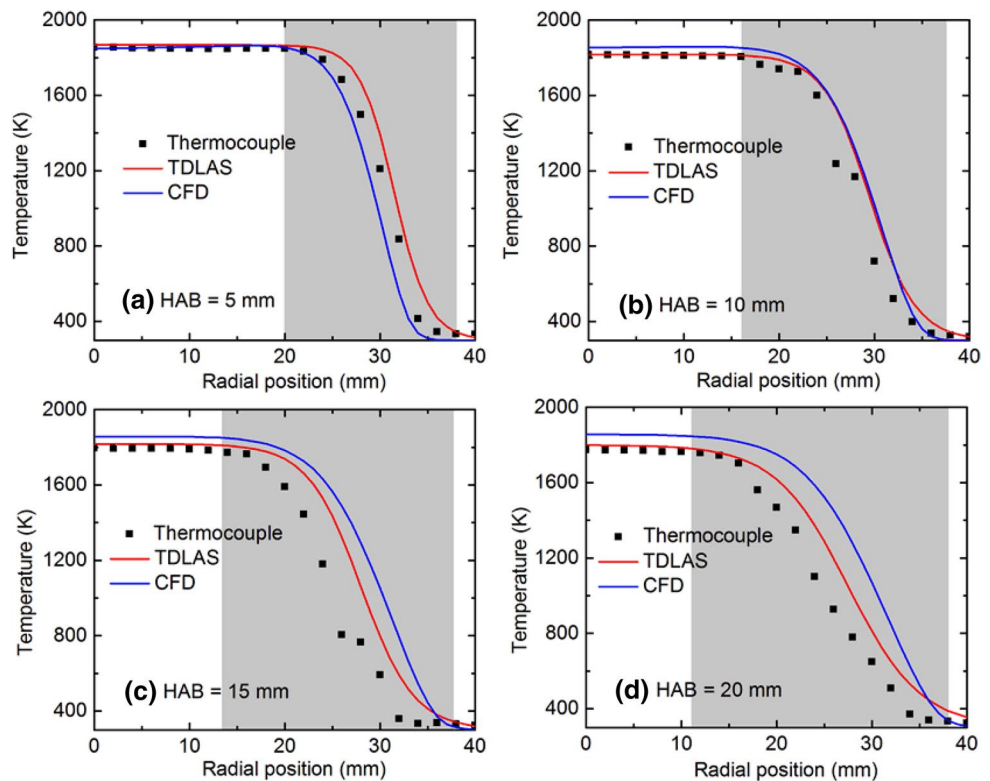
thermocouple result was estimated to have an uncertainty of approximately ± 100 K.

First, the central flame temperature is of particular interest to the combustion community because it is the region where chemical kinetics are normally studied [32]. Figure 6, thus, compares the measured central flame temperature at different HAB using TDLAS with the thermocouple measurement and the CFD simulation. According

to the TDLAS measurement, the central flame temperature decreases from 1868 K at HAB = 5 mm to 1800 K at HAB = 20 mm. Similar trends were observed for the thermocouple measurement and CFD simulation. The flame cools with the increase of HAB due to the radiation of high-temperature products to the surroundings with lower temperature. The TDLAS measurement of the central flame temperature is in excellent agreement with the thermocouple data at all HABs as demonstrated in Fig. 6. The maximum difference between the TDLAS and thermocouple measurement occurring at HAB = 20 mm is found to be within 30 K (<1.5%). The TDLAS measurement uncertainty of the central flame was evaluated mainly from the Voigt fitting and non-linear least square fitting errors. At HAB = 5 mm, the CFD simulation predicted a central flame temperature of 1864 K, in good agreement with the TDLAS (1868 K) and thermocouple (1854 K) measurements. However, with the increase of HAB, the CFD overpredicted the temperature gradually and reached a maximum difference of $\sim 2.2\%$ at HAB = 20 mm. Note that the flow rate monitored by the rotameter has an uncertainty of 2%, which may cause uncertainty in the boundary condition settings of the CFD simulation.

The measured radial distribution of temperature using TDLAS at various HAB positions is depicted in Fig. 7 with a comparison to the thermocouple measurement and the CFD simulation. The shaded region in Fig. 7 designates the

Fig. 7 Comparison of the radial temperature distribution obtained using TDLAS and thermocouple measurements with the CFD simulation at various HAB positions



range of the temperature gradient. The measurement and simulation exhibit that the radial temperature remains constant in the central region and then decreases to the ambient condition. The TDLAS measurements at HAB = 5 mm and 10 mm are in good agreement with the thermocouple data and the CFD simulation. At HAB = 5 mm, the uniform flame temperature in the central region starts to decrease at the position of 20 mm and reaches the ambient temperature at the position of 37 mm. At HAB = 10 mm, the central uniform region is narrowed and the transition position of temperature occurs at the radial position of 17 mm. When the HAB increases to 15 mm or even higher, the TDLAS and thermocouple measurements still have a relatively good agreement regarding the central uniform temperature and the transition position as illustrated in Fig. 7c, d. However, the thermocouple data in the gradient region (shaded in the figure) are consistently lower than the TDLAS measurements by a maximum relative difference of ~13%, i.e., approximately 200 K for the flame temperature of 1500 K at the radial position of 24 mm as shown in Fig. 7c. It should be noted that the thermocouple readout was unstable near the edge of the flame, which was analyzed due to the interrupted flow field and unstable heat transfer. At HAB = 15 and 20 mm, the CFD simulation overpredicted the temperature of both the central uniform flame and the gradient region.

A summarized 2-D map of the temperature distribution is illustrated in Fig. 8 to compare the TDLAS measurement with

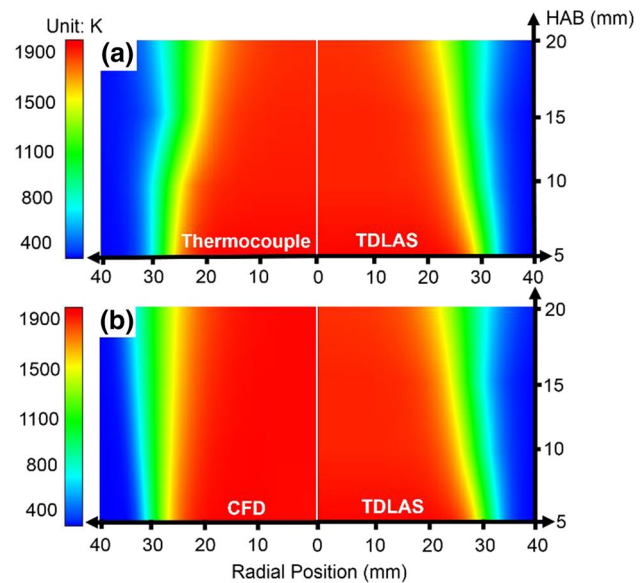


Fig. 8 2-D map of the flame temperature distribution. The TDLAS measurement is compared with (a) the thermocouple data and (b) the CFD simulation in the region of interest

the thermocouple data and the CFD simulation, respectively. The comparison made in Fig. 8a indicates that the TDLAS and thermocouple measurements capture the similar radial and axial distribution of the temperature in the laminar flame. However, the CFD simulation in Fig. 8b underestimates the

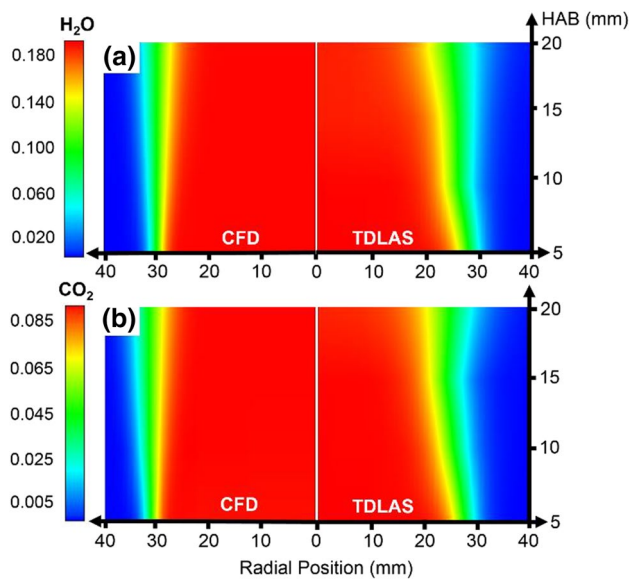


Fig. 9 2-D map of the species concentration distributions. The TDLAS measurement is compared with the CFD simulation for (a) H_2O and (b) CO_2

radial temperature gradient, particularly at the larger HAB. Note that our temperature measurement was conducted based on the fact that the radial flame temperature follows the Boltzmann distribution. Hence, the radial temperature distribution was directly determined when the parameters A_1 – A_3 and x_0 in Eq. (6) were determined by measuring multiple $\text{H}_2\text{O}/\text{CO}_2$ transitions along the line-of-sight. The 2D map of the TDLAS measured temperature shown in Fig. 8 is estimated to have a spatial resolution of 5 mm due to the current spatial sampling in the direction of HAB. This spatial resolution can be further improved by increasing the spatial sampling and reducing the laser beam size.

Finally, the measured H_2O and CO_2 concentration distributions using TDLAS are illustrated as a 2-D map in Fig. 9a, b, respectively. The H_2O and CO_2 concentrations in the central uniform region were measured to be 0.180 and 0.085, respectively, for the entire HAB varied from 5 to 20 mm. The CFD calculations were in excellent agreement with the TDLAS results (H_2O ~1.7%, CO_2 : ~5%) in terms of the species concentration in the central region. However, the CFD simulation underpredicted the H_2O and CO_2 gradients along the HAB compared with the TDLAS measurement, which has the similar trend as the temperature distribution discussed above.

5 Conclusions

The non-uniform distributions of temperature, H_2O and CO_2 concentrations were measured using multi-band

infrared absorption spectroscopy by employing two ICLs and one DFB diode laser. The Boltzmann fitting profile was adopted for the first time to characterize the distribution of temperature and species concentration above the laminar flame with axial symmetry. For comparison, the thermocouple measurement and CFD simulation were performed for the same laminar flame. In the central region of the flame with uniform temperature distribution, the maximum difference among the CFD simulation, TDLAS and thermocouple measurements was investigated to be ~2.2%. The TDLAS measured H_2O and CO_2 concentrations in the central flame region were in good agreement (H_2O : ~1.7%, CO_2 : ~5%) with the CFD values. The TDLAS well captured the decreasing tendency from the transition position to the ambient surroundings. Future work will involve the characterization of non-uniformity in the laminar flame with various cold boundary layer and equivalence ratio conditions.

Acknowledgements This research is supported by National Natural Science Foundation of China (NSFC) (11502222) and CUHK Direct Grant for Research.

References

1. C.A.Taatjes, N.Hansen, A.McIlroy, J.A.Miller, J.P.Senosiaian, S.J.Klippenstein, F.Qi, L.Sheng, Y.Zhang, T.A.Cool, *Science***308**(5730), 1887–1889 (2005)
2. F.N.Egolfopoulos, N.Hansen, Y.Ju, K.Kohse-Höinghaus, C.K.Law, F.Qi, *Prog. Energy Combust. Sci***43**, 36–67 (2014)
3. R.K.Hanson, D.F.Davidson, *Prog. Energy Combust. Sci***44**, 103–114 (2014)
4. S.Cheski, *Prog. Energy Combust. Sci***25**(3), 233–252 (1999)
5. J. H.Frank, P. A.Kalt, R. W.Bilger, *Combust. Flame***116**(1), 220–232 (1999)
6. J.Kiefer, F.Ossler, Z.Li, M.Aldén, *Combust. Flame***158**(3), 583–585 (2011)
7. S.Roy, J.R.Gord, A.K.Patnaik, *Prog. Energy Combust. Sci***36**(2), 280–306 (2010)
8. A.Cutler, P.Danehy, R.Springer, S.O', Byrne, D.Capriotti, R.Deloach, *AIAA. J.***41**(12), 2451–2459 (2003)
9. A. D.Cutler, L. M.Cantu, E. C.Gallo, R.Baurle, P. M.Danehy, R.Rockwell, C.Goyne, and J.McDaniel, *AIAA. J.***53**(9), 2762–2770 (2015)
10. M.E.Webber, J.Wang, S.T.Sander, D.S.Baer, R.K.Hanson, *Proc. Combust. Inst***28**(1), 407–413 (2000)
11. Z.Qu, R.Ghorbani, D.Valiev, F.M.Schmidt, *Opt. Express***23**(12), 16492–16499 (2015)
12. C.Liu, L.Xu, J.Chen, Z.Cao, Y.Lin, W.Cai, *Opt. Express***23**(17), 22494–22511 (2015)
13. F.Migliorini, S.Deluliis, F.Cignoli, G.Zizak, *Combust. Flame***153**(3), 384–393 (2008)
14. G.Hartung, J.Hult, C.F.Kaminski, *Meas. Sci. Technol***17**(9), 2485–2493 (2006)
15. X.Zhou, X.Liu, J.B.Jeffries, R.K.Hanson, *Meas. Sci. Technol***14**(8), 1459–1468 (2003)
16. C.S.Goldenstein, Ph.D.Thesis, (Stanford University, 2014)
17. X.Ouyang, P.L.Varghese, *Appl. Opt.***28**(18), 3979–3984 (1989)

18. S.T.Sanders, J.Wang, J.B.Jeffries, R.K.Hanson, *Appl. Opt.***40**(24), 4404–4415 (2001)
19. X.Liu, Ph.D. Thesis, (Stanford University, 2006)
20. X.Zhou, Ph.D Thesis (Stanford University, 2005)
21. G.Zhang, J.Liu, Z.Xu, Y.He, R.Kan, *Appl. Phys. B***122**(1), 1–9 (2016)
22. C.Liu, L.Xu, F.Li, Z.Cao, S.A.Tsekenis, H.McCann, *Appl. Phys. B***120**(3), 407–416 (2015)
23. L.Ma, W.Cai, A.W.Caswell, T.Kraetschmer, S.T.Sanders, S.Roy, J.R.Gord, *Opt. Express***17**(10), 8602–8613 (2009)
24. Q.Lei, Y.Wu, W.Xu, L.Ma, *Opt. Express***24**(14), 15912–15926 (2016)
25. L.Ma, Y.Wu, W.Xu, S.D.Hammack, T.Lee, C.D.Carter, *Appl. Opt.***55**(20), 5310–5315 (2016)
26. L.Xu, C.Liu, W.Jing, Z.Cao, X.Xue, Y.Lin, *Rev. Sci. Instrum.***87**(1), 013101 (2016)
27. R.K.Hanson, R.M.Spearrin, C.S.Goldenstein, *Spectroscopy and optical diagnostics for gases*(Springer, Berlin, 2015)
28. L.S.Rothman, I.E.Gordon, Y.Babikov, A.Barbe, D.C.Benner, P.F.Bernath, M.Birk, L.Bizzocchi, V.Boudon, L.R.Brown, J. Quant. Spectrosc. Radiat. Transf.**130**, 4–50 (2013).
29. R.M.Spearrin, W.Ren, J.B.Jeffries, R.K.Hanson, *Appl. Phys. B***116** (4), 855–865 (2014)
30. G.P.Smith, D.M.Golden, M.Frenklach, N.W.Moriarty, B.Eiteneer, M.Goldenberg, C.T.Bowman, R.K.Hanson, S.Song, W.C.GardinerJr, “GRI-Mech 3.0,” URL: http://www.me.berkeley.edu/gri_mech/. Accessed 18 Jan 2017
31. C.R.Shaddix, Proceedings of the 33rd National Heat Transfer Conference, Albuquerque, New Mexico, 15–17 Aug 1999
32. N.Hansen, T.A.Cool, P.R.Westmoreland, K.Kohse-Höinghaus, *Prog. Energy Combust. Sci.***35**(2), 168–191 (2009)